Metrol. Meas. Syst., Vol. 31 (2024), No. 2
DOI: 10.24425/mms.2024.149700

METROLOGY AND MEASUREMENT SYSTEMS
Index 330930, ISSN 0860-8229
www.metrology.wat.edu.pl

QUANTIFICATION OF MICROSTRUCTURAL HOMOGENEITY IN INDIUM ARSENIDE EPILAYERS BY X-RAY DIFFRACTION

Sebastian Odrzywolski[1)], Marek Andrzej Kojdecki[2)], Sebastian Złotnik[1)], Łukasz Kubiszyn[3)], Jarosław Wróbel[1)]

1) *Institute of Applied Physics, Military University of Technology, 2 Kaliskiego Street, 00-908 Warsaw, Poland*
2) *Institute of Mathematics and Cryptology, Military University of Technology, 2 Kaliskiego Street, 00-908 Warsaw, Poland* (✉ *marek.kojdecki@wat.edu.pl*)
3) *VIGO Photonics S.A., 129/133 Poznańska St., 05-850 Ożarów Mazowiecki, Poland*

Abstract

In this article a complete procedure to investigating thin semiconductor plates (epitaxial layers), including high-resolution X-ray diffraction measurements, mathematical modelling of both crystalline structure and crystalline microstructure and computations to approximate solving inverse problems, is proposed and described in detail. The methods is successfully applied to estimating crystalline homogeneity of square indium-arsenide plate epitaxially-grown on gallium-arsenide substrate. To this end the specimen is tested in nine areas around points forming square grid. It is demonstrated that whole specimen may be regarded as single large crystalline grain consisting of crystallites separated by small-angle boundaries. The crystallites occur rode-like cuboids elongated in direction perpendicular to plate surface, with heights very different in different areas of the sample and with base sizes not much differing. The mean-absolute second-order strain is very small and almost constant in whole sample. The first-order strain also appears and effectively the structure of the crystalline layer is tetragonal with unit-cell parameters being smaller parallelly and larger perpendicularly to the layer surface and varying slightly in the layer. The results are presented in tables and figures and commented.

Keywords: X-ray diffraction, crystalline structure, crystalline microstructure, epitaxy, indium arsenide, crystallite size, first-order strain, second-order strain.

1. Introduction

Indium arsenide (InAs) is a narrow bandgap binary compound (cubic with unit-cell constant of around 0.60580 nm), a representative of III-V semiconductor materials. These semiconductors have been widely used for optoelectronic devices, such as light emitters (light emitting diodes, laser diodes), transistors, electro-optical modulators, detectors *etc.* [1, 2]. In recent years, research and commercialisation in the area of infrared radiation detection, where InAs-based epilayers have been dominant to provide an alternative for HgCdTe, have been quite intensive [3-5].

In industrial technology of epitaxial materials, fast and non-destructive characterisation techniques play a very important role. One of them is high-resolution X-ray diffractometry, being used in science and industry for many years in the design of novel structures and quality control [6, 7]. One of the advantages of high-resolution X-ray diffractometry is the rapid collection of data. In contrast, limitations are the need for an accurate approach to the measurements, and especially to the analytical procedure [6]. This technique allows obtaining information on: structural homogeneity of the studied materials, stress state, mosaic microstructure growth, dislocation density, surface damage [8-11]. In the case of III-V superlattices studies, it allows estimating their composition, thickness and period [12, 13].

Article history: received September 4, 2023; revised December 28, 2023; accepted February 7, 2024; available online March 25, 2024.

In terms of microstructural features, there are two different forms of microstructure description. The first one refers to domains with a high level of structural homogeneity (crystallites and crystalline grains). The second one refers to disorder of lattice, *i.e.* defects [14, 15]. In the first approximation, a crystal is considered to be a collection of crystallites. Each crystallite may be a crystalline grain or a mosaic block that is a part of a grain. Most often, crystallites have regular and similar shapes resulting from similar growth conditions [14]. The most common parameters of crystalline microstructure are size, shape and deformation of crystallites. The crystallite size distribution may be interpreted as the density of probability of finding a crystallite with an assumed shape and size (usually taken with the weight proportional to the volume, or surface, or linear dimension) in an analysed sample. The shape of crystallites, when modelled as simple solids, may be described by aspect ratios of characteristic dimensions, called also shape factors or shape coefficients. In general, it is assumed that crystallites show high structural homogeneity, but differ in their lattice parameters. To describe the variation of lattice parameters, a second order strain distribution of crystalline lattice was introduced. This distortion distribution may be interpreted as the density of probability of finding a crystallite in which the interplanar distances differ in an assumed value from those of the reference crystallite. The reference crystalline lattice is the average of all crystallites. The distribution of deformations (second-order strain) may be assumed to not depend on the size of crystallites and to be statistically isotropic [16-18]; it means that although strains are considered there [16-18] as homogeneous but in general anisotropic inside each single crystallite, the second-order strain distribution only is considered as isotropic (same in all crystal directions). Most industrial materials should be considered as polycrystals. Even semiconductor wafers, usually considered as monocrystals, are frequently defected by dislocations and may be effectively interpreted as single mosaic blocks with crystallites slightly misoriented one another – or as polycrystals with strong texture.

Principal phenomenon exploited to reveal both crystalline structure and crystalline microstructure is *X-ray diffraction* (XRD). The determination of structure characteristics (unit-cell constants first of all) is based of measurements of positions of peaks in XRD pattern that correspond to Bragg diffraction angles; with exploiting peak intensities it also possible to determine positions of atoms inside unit-cell. The determination of microstructure characteristics is based on the observation that the line profiles (or peak shapes), contributing to XRD pattern, depend on them. Several methods, in which different, more or less simplified, mathematical models of this relation were applied, have been proposed. The contribution from instrumental factors to XRD line profiles should be additionally accounted for to estimating microstructure parameters reliably. In fact, the pure (or physical) XRD line profiles, obtained from the experimental ones through correction of background and instrumental contribution, are analysed to characterise the microstructure. These pure line profiles may be interpreted as being produced from perfectly monochromatic and parallel X-ray beam. The information on crystalline microstructure of an investigated specimen is hidden in them and particularly in the full-widths-at-half-maximums (peak widths). Generally, the smaller the crystallites or the larger the second-order strain, the broader the peaks.

The Williamson-Hall method [19-24] is based on the use of simplified formulae for the width of XRD line profile from a perfect crystallite as dependent on its size and shape (Scherrer formula) and for the broadening that results from the second-order strains (Wilson-Stokes formula). This method uses only widths of line profiles and assumes that these profiles are Cauchy (Lorentz) functions, which is generally not true. The advantage of the Williamson-Hall method is the inclusion of deformations, while the disadvantages are still the incorrect assumption on line profile functions (even in such complex analysis as performed by Magalhães [24]). Another popular approach is the Warren-Averbach-Bertaut method [25-31]. It allows to find the average size of crystallites, their size distribution and the characteristics of second order

strains (and stresses). Among the disadvantages of this method there is the inaccuracy in the original formulation. Instead of the distribution of crystallite size, the column length distribution of elementary units in crystallites are used. In addition, a limitation of the Warren-Averbach-Bertaut method is the lack of physical interpretation of the function characterising second-order deformations. The next one is the Balzar method, developed taking into account the size and shape distribution of crystallites. Balzar [28, 29, 31, 32] assumed a theoretical description of the line profile - in modelling the experimental data, but he proposed only the spherical shape of the crystallites and assumed in advance the form of the crystallite size distribution function. Balzar's method is valid mainly for cubic materials. Other methods are those of Louër and Langford [33-36] and Scardi and Leoni [37-41]. They developed methods taking into account the size distribution of crystallites and their shape. In addition, they assumed a theoretical description of line profiles. Louër-Langford's method was used successfully for various crystallite shapes, but only for materials in which the second-order deformation and scattering of crystallite sizes could be neglected. In contrast, Scardi-Leoni's modelling assumed in advance a spherical shape of crystallites and a crystallite size distribution function. In addition, the second order deformation and dislocation density distribution were taken into account. The method is valid mainly for cubic materials. A very similar method was developed by Cervellino [42-45]. Some of these methods are quite general; they make it possible to find detailed microstructure characteristics but with the strongly simplifying assumption that crystallites are spheres [38, 42]. The method [48] used in this paper contains no such strong simplification although is still simplified version of a more general one [14-18].

In the present study, the crystalline homogeneity of the indium arsenide epitaxial layer was investigated using the *high-resolution XRD* (HRXRD); a method using a more realistic model of the crystal microstructure was applied. The purpose of the study was to evaluate the structural and microstructural homogeneity in different parts of the semiconductor wafer. The comparison criterion was the averaged parameters of the crystalline structure – the unit-cell parameters and of the crystalline microstructure – the lengths of edges of the mean crystallite (modelled as cuboid) and the mean-absolute second-order lattice strain.

2. Materials and method

2.1. Indium arsenide epilayer sample and high-resolution X-ray diffraction equipment

A 5.15μm-thick non-dopped InAs epitaxial layer was deposited by molecular beam epitaxy (MBE) on a circular 2-inch GaAs substrate with a 2° offcut. The specification of the MBE system can be found elsewhere [46, 47]. Before the growth process the substrate was degassed to thermally desorb the oxides. A GaAs buffer layer of 0.25 μm thickness was deposited prior to InAs. The process was strictly controlled and monitored using reflection high-energy electron diffraction which confirmed a Stranski-Krastanov growth mode. As a result, the normal to the plate surface coincides with $[001]$ crystal direction. The almost-square sample with edge length of 20 mm was then cut from this wafer.

InAs specimen were investigated using a high-resolution PANalytical X'Pert3 MRD diffractometer, working at 45 kV and 30 mA, equipped with a copper X-ray tube, a channel-cut 4X Ge(004) monochromator in incident beam and PIXcel^{1D}-Medipix 3 detector used as a point detector for measurements of rocking curves and as a line detector for measurements of diffractograms. The rocking curves (ω-scans, with scanning step of $0.001°$) and diffraction line profiles ((2θ-ω)-scans, with scanning step 2θ of $0.00123°$) originating from sets of crystal planes (002), (004), (115), (135), (006), (335), (226), corresponding to (2θ) diffraction Bragg angles 29.4532, 61.1165, 82.6683, 97.5200, 99.3917, 112.9145, 114.9399 (for cubic crystalline lattice with $a = 0.606040$ nm determined in this work; $\lambda = 0.1540597$ nm) were

recorded; the positions and intensities of XRD peak maxima are collected in Table 1. The ω-curves made it possible to infer the crystalline quality of the tested indium arsenide plate. In turn, the (2θ-ω) curves were used to determine the unit-cell constants and the averaged parameters of the crystalline microstructure. A point grid was applied to the test sample (as shown in Fig. 1) and measurements were taken at small areas around each point with 6 mm apart one another.

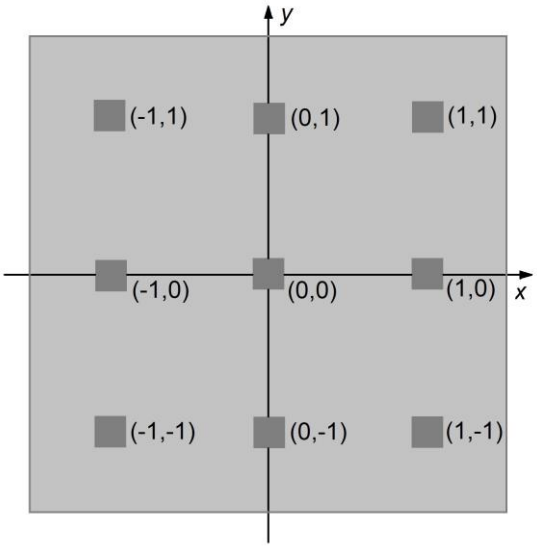

Fig.1. Locations of square measurement areas (with limits not marked) on the sample (indium arsenide thin near-square plate of edge length of around 20 mm) with coordinates of their centres (related to 6 mm units in both directions).

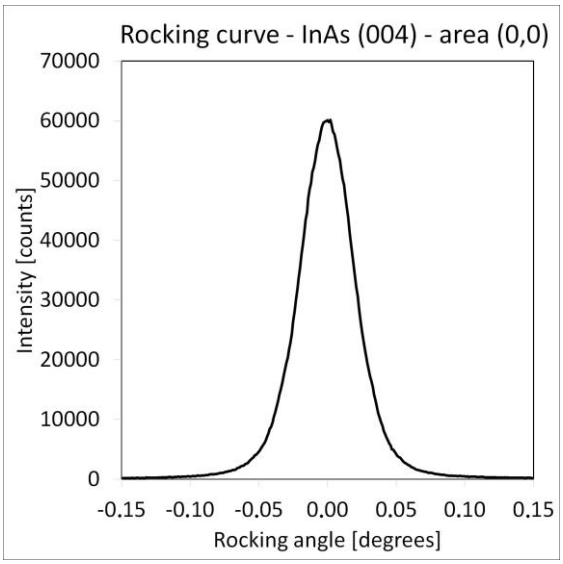

Fig. 2. The measured rocking curve related 004 reflexion at the central area $(0,0)$ of the specimen.

Table 1. Positions and intensities of maxima of XRD line profiles recorded for nine areas of indium arsenide specimen.

Area	002	004	115	135	006	335	226
	θ_0 [°]	θ_0 [°]	θ_0 [°]	θ_0 [°]	θ_0 [°]	θ_0 [°]	θ_0 [°]
	I_0	I_0	I_0	I_0	I_0	I_0	I_0
(-1,1)	14.73351	30.56101	41.33979	48.78553	49.69274	56.49364	57.48188
	7526	19964	4587	4465	259	2489	210
(0,1)	14.73390	30.56167	41.34095	48.78068	49.69331	56.49654	57.48270
	7517	19635	4577	2421	271	1860	248
(1,1)	14.73462	30.56221	41.34123	48.78338	49.69342	56.49927	57.48150
	7705	19786	4665	2622	270	1885	261
(-1,0)	14.72586	30.55382	41.33189	48.77512	49.68755	56.48969	57.47896
	10593	23013	4321	2854	253	1774	224
(0,0)	14.72674	30.55497	41.33373	48.77857	49.68924	56.48931	57.47819
	10203	22203	4273	2789	261	1992	235
(1,0)	14.72719	30.55518	41.33512	48.78049	49.68845	56.49138	57.47800
	10926	23167	4359	2795	262	1898	224
(-1,-1)	14.72799	30.55574	41.33493	48.77697	49.68850	56.48716	57.47830
	9902	22177	4368	3496	260	2065	231
(0,-1)	14.72871	30.55637	41.33581	48.77874	49.68927	56.48946	57.47881
	10451	22996	4454	3605	259	1937	245
(1,-1)	14.72938	30.55679	41.33691	48.78008	49.68889	56.48872	57.47953
	10682	22770	4372	2475	275	2067	241

2.2. Structure evaluation

Indium arsenide is well known as cubic crystal with unit-cell constant a around $0.60580\ \mathrm{nm}$ [56]. The thin plate of indium-arsenide with crystal planes (001) oriented parallelly to the planar surface, like in this work, is frequently deposited on the planar substrate of gallium-arsenide of the same type of crystal lattice and orientation but with smaller (of a 7%) constant a around $0.56537\ \mathrm{nm}$. Therefore it is reasonable to admit strong shear stresses along contact surface causing permanent deformation (first-order strain) inside the studied sample resulting in establishing pseudo-tetragonal structure and appearing dislocations. To characterise crystalline structure the unit-cell parameters are found for crystalline lattices of both types.

The unit-cell constants (a or a, c) may be reliably computed from experimental Bragg angles by exploiting simultaneously several recorded XRD peaks involving reflexions from set of planes hkl with non-zero Miller indices in all positions. When HRXRD is applied the experimental Bragg angles may be precisely determined as positions $\theta_{0,hkl-m}$ of maximums of XRD line profiles (measured) and from them the experimental interplanar distances may be found:

$$d_{hkl-m} = \frac{\lambda}{2 \bullet \sin(\theta_{0,hkl-m})}\,. \tag{1}$$

On the other hand these distances may be calculated given unit-cell constants and reflexion indices:

$$d_{hkl-c} = \frac{a}{[h^2 + k^2 + l \bullet \frac{a}{c}^{\,2}]^{\frac{1}{2}}} \tag{2}$$

(for cubic lattice $a = c$, for tetragonal one $a \neq c$).

Then the lattice parameters and all reflexion indices are together calculated from experimental data (m peaks) as minimiser to the similarity functional:

$$\psi(a,c;h,k,l)=\left[\frac{1}{m}\sum\nolimits_{hkl}\left(\frac{d_{hkl-m}-d_{hkl-c}}{d_{hkl-m}}\right)^2\right]^{\frac{1}{2}} \tag{3}$$

being root-mean-square relative error of approximating the experimental interplanar distances by the modelled ones.

2.3. Microstructure evaluation

The following assumptions are considered for the mathematical model of a crystal interpreted as a set of crystallites:

- all crystallites are of the same size and shape, forming a monodisperse set of grains or mosaic blocks;
- each crystallite is modelled as cuboid (or rectangular prism) with edges and faces parallel or perpendicular to main crystal axes and with square base;
- each crystallite is a perfect monocrystal with unit-cell constants which may differ from the crystal mean values;
- a second-order strain distribution (or a unit-cell constant distribution) is normal;
- a diffractogram is formed by a monochromatic and parallel radiation beam, and the kinematic theory of X-ray scattering is sufficient to describe it.

The second-order strain is considered as homogeneous (although possibly anisotropic) inside each crystallite and statistically isotropic. Each crystallite is considered to be strained in such way that along a specific crystal direction the interplanar distance in it is equal to d instead of to the mean for whole specimen d_0; then the corresponding strain is equal to $e=\frac{d-d_0}{d_0}$ and it is accounted in the second-order strain distribution with the weight proportional to the crystallite volume. The distribution of deformations (second-order strain) is assumed to not depend on the size of crystallites and to be statistically isotropic [16-18] (being the same along each crystal direction); it means that although strains are considered as homogeneous but in general anisotropic inside each single crystallite, the second-order strain distribution only is considered as isotropic (same in all crystal directions).

When the second-order strain (*i.e.* randomly distributed deformations of crystalline lattice being homogeneous inside each crystallite and related to average lattice parameter same as in unstrained material) coexists with the first-order strain (*i.e.* permanent deformation cause by external forces that may cause change of average lattice parameters, differently in monocrystals and in polycrystalline materials) both effects may be studied with use of XRD but involving different mathematical models as well as measurement methods and computational procedures.

The total full-width-at-half-maximum (FHWM; 'width' further in this work) of a pure line profile, $w_{f,hkl}$, depends on contributions from a second-order strain, $w_{r,hkl}$, and a set of crystallites, $w_{k,hkl}$. For a monodisperse population of crystallites the same width, $w_{c,hkl}$, comes from all crystallites, thus $w_{k,hkl}=w_{c,hkl}$. The $w_{r,hkl}$ and $w_{c,hkl}$ and $w_{k,hkl}$ for (hkl) reflexion can be described by approximate formulae [48]:

$$w_{r,hkl}=2\sqrt{2\ln 2}\bullet\sqrt{\tfrac{\pi}{2}}\bullet e\bullet \mathrm{tg}(\theta_{0,hkl}) \tag{4}$$

$$w_{c,hkl}=\left[\frac{1-\frac{1}{2}(\frac{H+K+L}{F})+\frac{1}{3}(\frac{HK+HL+KL}{F^2})-\frac{1}{4}(\frac{HKL}{F^3})}{\frac{1}{3}-\frac{1}{4}(\frac{H+K+L}{F})+\frac{1}{5}(\frac{HK+HL+KL}{F^2})-\frac{1}{6}(\frac{HKL}{F^3})}\right]^{\frac{1}{2}}\frac{F}{\sqrt{G}}\ \bullet\ \frac{0.584\bullet\lambda}{\pi\bullet a\bullet\cos(\theta_{0,hkl})}\ \bullet\ \frac{1}{n} \tag{5}$$

$$w_{k,hkl}=\left(1-0.25\,\frac{\sigma}{\mu}\right)\bullet w_{c,hkl} \tag{6}$$

$$w_{f,hkl}(w_{k,hkl}, w_{r,hkl}) = \begin{cases} \left[-0.189358 \bullet \left(\frac{w_r}{w_k}\right)^3 + 0.700940 \bullet \left(\frac{w_r}{w_k}\right)^2 - 0.070257 \bullet \left(\frac{w_r}{w_k}\right) + 1\right] \bullet w_k & \text{for } w_r \le w_k \\ \left[0.069441 \bullet \left(\frac{w_k}{w_r}\right)^3 + 0.106305 \bullet \left(\frac{w_k}{w_r}\right)^2 + 0.275051 \bullet \left(\frac{w_k}{w_r}\right) + 1\right] \bullet w_r & \text{for } w_k \le w_r \end{cases} \quad (7)$$

where $e = \sqrt{\frac{2}{\pi}}\varepsilon$ – is the mean-absolute second-order strain of crystalline lattice (throughout the crystal, when normal strain distribution with zero mean and standard deviation ε with mean deviations e is assumed); $\theta_{0,hkl}$ is the Bragg angle; σ, μ are the standard deviation and expected value for the crystallite size distribution (in this work it is finally assumed that $\sigma = 0$, as for monodisperse population of crystallites). For cubic system, $H = h,\ K = k,\ L = \kappa^{-1}l$, $G = h^2 + k^2 + l^2,\ F = \max\{H, K, L\}$, were h, k, l are Miller indices, a – is the unit-cell constant, $n \bullet a = \mu$ – is the average crystallite size (length of the edge of square base of a cuboid in directions [100] and [010]), κ – is the form factor (defining height of cuboidal crystallite in [001] direction, equal to $\kappa \bullet n \bullet a$ for cubic crystal or $\kappa \bullet n \bullet c$ for tetragonal crystal, with respect to base edge length); the only difference in these formulae for tetragonal system is $L = \kappa^{-1}\frac{a^2}{c^2}l$. The width w_f of line profiles are expressed in approximate formulae (4-7) based on simulation of whole XRD line profiles with accounting for a normal second-order strain distribution with parameters $(0, \varepsilon)$ (as described above) and a logarithmic-normal cuboidal crystallite volume-weighted size distribution with parameters (σ, μ) [48]. In this way, the crystalline microstructure, on average, is characterised by the set of parameters: n, κ, e, σ and derivative quantities, while the widths of corresponding pure line profiles are expressed by formulae (4-7) as the functions of these parameters. Subsequently, to characterising a real polycrystal such values of these parameters should be found for which the discrepancy between the sets of pure line profile widths measured (determined from XRD patterns) and simulated (according to formulae (4-7)) is as small as possible. In finding the parameters the root-mean-square relative error of approximation was used as a criterion of similarity:

$$\varphi(n, \kappa, e, \sigma) = \left[\frac{1}{m}\sum_{hkl}\left(\frac{w_{f,hkl-m} - w_{f,hkl-c}}{w_{f,hkl-m}}\right)^2\right]^{\frac{1}{2}} \quad (8)$$

where m is the number of simultaneously analysed line profiles, $w_{f,hkl-m}$ is the width (FWHM) of a pure line profile calculated from measurements, $w_{f,hkl-c}$ is the width of a pure line profile calculated from (4-7).

More complete characteristics of crystalline microstructure including crystallite size distribution and second-order strain distribution can be found from diffractograms with no prior assumptions by more complex method [14-18].

3. Results and discussions

3.1. Idea and interpretation of measurements

Two modes of measurements were applied with using the mentioned above diffractometer specialised to investigating semiconductor monocrystalline plates. This diffractometer features vertical specimen stage and operating mode with fixed position of X-ray tube.

The rocking curve (ω-scans) is recorded when the sample rotates (at ω angle) in both directions around the axis lying at the sample surface, perpendicular to diffraction plane, with fixed position of the detector (*i.e.* with fixed (2θ) diffraction Bragg angle between the tube arm and the detector arm); the position of XRD line profile maximum results at $\omega = 0$. The rocking

curve provides the information on spatial distribution of orientations of crystallites with respect to the considered crystallographic direction; especially the narrower the peak the less scattered the orientations of crystallites.

The diffractogram ((2θ-ω)-scans – X-ray diffraction pattern) is recorded when both the sample and the detector rotate in the same direction with preserving the same angle between each arm and the sample surface normal or diffracting plane normal ($\Delta\omega = \Delta\theta$); when each line profile is recorded separately, such initial sample slope ω is chosen that both the angles between the tube arm or the detector arm and the normal to diffracting planes are equal and close to (θ) reflexion Bragg angle. In this way, when a sample is monocrystalline (possibly with inner mosaic structure featuring strong texture), each recorded XRD line profile may be assigned to a family of diffracting crystal planes the orientation of which with respect to the sample normal is uniquely defined. The diffractogram provides the information on crystalline structure (in positions of radiation intensity maximums approximating Bragg angles, together with peak intensities) and on crystalline microstructure (in shapes of line profiles); especially the narrower the peak the larger and less strained the crystallites.

3.2. Shapes of measured line profiles

The XRD line profiles after background subtraction sometimes may be well approximated as some specific functions (plane curves) with simple formulae. Such approximation may be exploited to smooth profiles and determine the width (FWHM) of profiles and to extract pure line profiles from pairs of experimental and standard ones (in special cases, as described below in chapter 3.5). In the present study, as frequently in XRD measurements, the line profiles, as well as rocking curves, occurred to be very close to Voigt functions and this approximation was exploited to estimate and compute widths of experimental, standard and pure line profiles.

All background-corrected experimental XRD line profiles (after subtraction of background) were approximated (by applying least-squares method) as the Voigt functions:

$$f_V(x) = A\,\frac{2\ln 2}{\pi^{3/2}}\,\frac{w_L}{(w_G)^2}\int_{-\infty}^{\infty}\frac{e^{-t^2}}{\left(\sqrt{\ln 2}\,\frac{w_L}{w_G}\right)^2+\left(\sqrt{4\ln 2}\,\frac{x-x_c}{w_G}-t\right)^2}\,dt\,, \tag{9}$$

each of them being the convolution of two components, the Gauss function and the Lorentz (or Cauchy) function, in standard forms:

$$f_G\ x\ = \sqrt{\frac{4\ln 2}{\pi}}\,\frac{1}{w_G}\ \exp\left(-\frac{4\ln 2\ x-x_c\ ^2}{(w_G)^2}\right), \tag{10}$$

$$f_L\ x\ = \frac{2A}{\pi}\,\frac{w_L}{4\ \ x-x_c\ ^2+(w_L)^2}\ \ , \tag{11}$$

where A – is the area between the graph and abscissa axis, x_c – is the position (abscissa) of maximum (centre of line profile), w_G, w_L – are FWHMs of both components; the total width of line profile was then computed from approximate formula:

$$w_V = 0.5346 \bullet w_L + \sqrt{0.2166 \bullet {w_L}^2 + {w_G}^2}\,. \tag{12}$$

The approximation of XRD line profiles as Voigt functions with such decomposition was performed by solving non-linear least squares problems with using Origin software.

3.3. Rocking curves and texture in indium arsenide plate

The rocking curves were recorded separately in relation to seven analysed reflexions for all nine areas of the specimen. The sample was rocked around position of maximum intensity in which the angle between the tube and detector arms was fixed to diffraction (2θ) Bragg angle. Each experimental position of peak maximum agreed within $0.04°$ of reflexion (θ) angle with a Bragg angle computed for Cu K_{α_1} wavelength ($\lambda = 0.1540597$ nm) and approximate unit-cell constant $a = 0.60580$ nm as well $a = 0.60604$ nm determined in this work. The sample was positioned with the angle τ between the normal to diffracting crystal planes and the normal to sample surface (coinciding with direction $[001]$) as small as possible; in this way last index l of each set of diffracting planes hkl was determined uniquely. The results of measurements and calculations are collected in Table 2. As an example, the rocking curve related reflexion 004 recorded from the central area $(0,0)$ of the sample is shown in Figure 2; the others are almost undistinguishable when presented in the same diagram. The line profiles of rocking curves are Voigt-function-type with Gauss-function-type component dominating, as it is illustrated, as an example, in Table 3 for curves recorded for all areas and related 004 reflexion. They are typical of polycrystalline material without effects specific for monocrystals, what can be interpreted as evidence of at least mosaic microstructure of the investigated specimen – the indium arsenide plate occurs to be a monocrystal with defects resulting in formation of crystallites slightly misoriented each other. Very narrow rocking curves evidence strong texture in all studied directions characterised by the angle τ between the normal to sample plate surface and the normal to diffracting crystal planes with fixed index l (Table 2), that confirm the previous prediction. The widths of all curves vary around $\delta = 0.05°$. Considering edge dislocation producing such mutual inclination of two vicinal crystallites one can estimate the crystallite size in direction perpendicular to Burgers vector as equal to $\frac{a}{\delta} \approx \frac{0.60580}{0.00087}\text{nm} \approx 700\text{nm}$; this estimate agrees with one of microstructural characteristics of the specimen (presented further).

Table 2. The widths w_ω of measured rocking curves derived for seven reflexions 004, 004, 115, 135, 006, 335, 226 corresponding to Bragg angles θ_0 (for cubic lattice of approximate $a = 0.60580$ nm and $\lambda = 1.540597$ nm) for nine measurement areas of the indium arsenide plate; the angle τ between the normal to the sample surface (coinciding with [001] direction) and the normal to diffracting crystal planes with uniquely determined index l are added.

hkl	002	004	115	135 - 315	006	335	226
θ_0 [°]	14,7326	30,5717	41,3542	48,7860	49,7227	56,4917	57,5058
τ [°]	0,0000	0,0000	15,7932	32,3115	0,0000	40,3155	25,2394
Area	w_ω [°]	w_ω [°]	w_ω [°]	w_ω [°]	w_ω [°]	w_ω [°]	w_ω [°]
(-1,1)	0.0464	0.0477	0.0455	0.0505	0.0517	0.0474	0.0501
(0,1)	0.0464	0.0475	0.0457	0.0426	0.0507	0.0453	0.0518
(1,1)	0.0463	0.0477	0.0456	0.0432	0.0511	0.0458	0.0528
(-1,0)	0.0456	0.0455	0.0436	0.0427	0.0486	0.0450	0.0501
(0,0)	0.0457	0.0457	0.0435	0.0426	0.0493	0.0445	0.0494
(1,0)	0.0462	0.0464	0.0444	0.0431	0.0496	0.0451	0.0507
(-1,-1)	0.0458	0.0462	0.0445	0.0429	0.0499	0.0448	0.0504
(0,-1)	0.0458	0.0460	0.0443	0.0426	0.0492	0.0441	0.0504
(1,-1)	0.0455	0.0462	0.0441	0.0425	0.0505	0.0444	0.0502

Table 3. The widths of Voigt functions (same as in corresponding column of Table 2) together with widths of Gauss-function and Lorentz-function components approximating rocking curves related 004 reflexion for all measurement areas and reliability factors.

Area	w_G [°]	w_L [°]	w_V [°]	R^2
(-1,1)	0.0393	0.0146	0.0477	0.9998
(0,1)	0.0391	0.0145	0.0475	0.9998
(1,1)	0.0395	0.0142	0.0477	0.9998
(-1,0)	0.0375	0.0140	0.0455	0.9998
(0,0)	0.0376	0.0140	0.0457	0.9998
(1,0)	0.0382	0.0142	0.0464	0.9998
(-1,-1)	0.0380	0.0143	0.0462	0.9998
(0,-1)	0.0377	0.0143	0.0460	0.9998
(1,-1)	0.0380	0.0144	0.0462	0.9998

3.4. Reference material and instrumental correction

The XRD standard line profiles are necessary for extracting the pure line profiles from the experimental line profiles. They must represent whole instrumental contribution from X-ray source and all slits, collimators and monochromators, both from the source and the detector side, shaping the X-ray beam in a diffractometer. They may be produced via immediate measurements of XRD patterns from a reference material same as the studied one but containing crystallites sufficiently large, unstrained and randomly oriented which contribute to line profiles negligibly. Especially the spatial distribution of the orientations of crystallites in the reference sample should imitate the distribution in the investigated sample. In lack of such material some standard reference material may be exploited to construct the instrumental function and to produce the standard line profiles corresponding exactly to Bragg angles for the studied sample [49].

In this work the special case of the defected monocrystalline material is studied. It can be treated in modelling and computations as polycrystalline one but with very narrow dispersion of orientations of the crystallites (strong texture). Hence the monocrystalline silicon plate (NIST SRM 2000) was used as standard reference material (SRM) to estimate the instrumental contribution to the experimental line profiles. This SRM is dedicated principally as the standard (cubic, with $a = 0.5431035$ nm) to precise determination of unit-cell constants by exploiting Si 004 reflexion (with very precisely determined interplanar distance d_{022} [50]). A unit of SRM 2000 consists of 25 mm $\times 25$ mm $\times 0.725$ mm double-polished (001)-oriented single-crystal silicon (Si) specimen with a nominal 50 nm $\mathrm{Si}_{0.85}\mathrm{Ge}_{0.15}$ epitaxial layer and 25 nm Si cap [51].

The measurements were performed with applying four-fold germanium 4X Ge(004) incident beam monochromator which cut only the central part of the Cu K_{α_1} spectral line; according to the diffractometer specification, for Si 004 reflexion the width (2θ) of the line profile is less than $0.0021°$ while the width of the line profile from only Cu K_{α_1} component (without accounting for additional broadening caused by slits) would be $0.02305°$, as it follows from Cu K_α radiation characteristics [52, 53]. It results in very narrow XRD line profiles as it is shown in Table 4; the widths of XRD line profiles from silicon plate (SRM 2000) recorded both with front surface (from deposited thin layer face) up or back surface (from thick silicon substrate face) up, together with the width of XRD line profiles from indium arsenide specimen recorded at the plate centre $0,0$, are given to compare. Only line profiles were important and therefore any procedure of precise measurements like described in SRM 2000 certificate [51] was not applied. The measurements were performed with the angle ω_0 of initial specimen slope respect to position with right angle (for Si) or Bragg angle (for InAs) between X-ray tube arm and the specimen surface; in this way the effective angle between the source arm and diffracting crystal planes hkl with uniquely determined index l and the angle τ between the normal to these planes and the normal to the sample surface coinciding with [001] direction, equal $\tau +$

ω_0, was close to appropriate Brag angle (Table 4). The widths of rocking curves from the silicon standard sample occurred very narrow and much narrower than those from the investigated indium arsenide sample, that evidenced crystalline order close to monocrystalline. It supports the use of SRM 2000 to estimating the instrumental contribution to experimental line profiles from indium arsenide. Nevertheless the XRD peaks were typical of polycrystalline materials with peak widths varying strongly with the dependence on Bragg angle that could hardly be explained, what suggested the contribution from crystalline microstructure. Since a detailed study of microcrystalline properties of the silicon standard is not a goal of this work, they served only to estimating the standard line profiles. The estimation is based on the observations that these line profiles are Gauss functions (in good approximation) and almost half of line profiles are of similar width varying in the range (2θ) from 0.0262 to 0.0342 degrees, while for the indium arsenide specimen the narrowest Gauss-function component of experimental line profiles (of 002 reflexion) is around (2θ) 0.0190 degrees. Moreover, in view of very narrow spectral distribution of radiation the instrumental function is dominated by a component independent of Bragg angle [50]. Taking all these facts and results of numerical experiments into account, we have chosen the Gauss function with width of $0.01203°$ (2θ) (equal to (θ) 0.000105 rad), as standard line profile independent of Bragg angle. It was further used to perform the instrumental correction of experimental XRD patterns from the investigated specimen.

All measurements were effective only with so narrow and highly monochromatic X-ray beam as it was at the disposal in this diffractometer with arrangement specially designed and dedicated just for such analyses; they would be impossible with using standard diffractometer due to very narrow pure line profiles from indium arsenide specimen and then very small difference between experimental and standard line profiles resulting in pure line profiles dominated by noise.

Table 4. The widths of Voigt functions w_V together with widths of Gauss-function and Lorentz-function components w_G, w_L and reliability factors R^2 approximating XRD line profiles measured from silicon standard reference unit (cubic, $a = 0.5431035$ nm) positioned with thin layer cap up (top table – front face) and with bulk silicon plate up (middle table – back face) and XRD line profiles measured from middle area $(0,0)$ of indium arsenide specimen (cubic, approximately $a = 0.60580$ nm; bottom table) with using highly-monochrome Cu K_{α_1} radiation ($\lambda = 1.54056$ nm); the Bragg angles θ_0 correspond to precise values od unit-cell constant and wavelength; τ is the angle between the normal to the sample surface (coinciding with [001] direction) and normal to diffracting crystal planes (hkl) with index l uniquely determined (as shown), ω_0 is the angle of initial specimen slope respect to position with right angle (for Si) or Bragg angle (for InAs) between X-ray tube arm and the specimen surface, w_ω are the width of corresponding rocking curves (all widths are given in diffraction angle 2θ scale). The narrowest widths are bolded.

Si hkl f	θ_0 [°]	τ [°]	ω_0 [°]	$\omega_0 + \tau$[°]	w_ω [°]	w_G [°]	w_L [°]	w_V [°]	R^2
113	28.0605	25.2394	2.6035	27.8429	0.0053	0.2638	0.0000	0.2638	0.9997
004	34.5641	0.0000	34.3359	34.3359	0.0022	**0.0324**	0.0011	**0.0330**	0.9966
224	44.0138	35.2644	8.5282	43.7926	0.0086	0.0967	0.0000	0.0967	0.9948
115	47.4748	15.7932	31.4658	47.2590	0.0112	**0.0263**	0.0000	**0.0263**	0.9987
044	53.3525	45.0000	8.2267	53.2267	0.0178	0.1044	0.0000	0.1044	0.9985
026	63.7696	18.4349	45.2072	63.6421	0.0356	**0.0255**	0.0012	**0.0262**	0.9974
335	68.4433	40.3155	27.9179	68.2334	0.0470	**0.0292**	0.0000	**0.0292**	0.9958

Si hkl b	θ_0 [°]	τ [°]	ω_0 [°]	$\omega_0+\tau$ [°]	w_ω [°]	w_G [°]	w_L [°]	w_V [°]	R^2
113	28.0605	25.2394	2.6084	27.8478	0.0045	0.2835	0.0000	0.2835	0.9990
004	34.5641	0.0000	34.3461	34.3461	0.0022	**0.0342**	0.0000	**0.0342**	0.9957
224	44.0138	35.2644	8.5360	43.8004	0.0088	0.0953	0.0000	0.0953	0.9953
115	47.4748	15.7932	31.4679	47.2611	0.0115	**0.0268**	0.0000	**0.0268**	0.9992
044	53.3525	45.0000	8.1106	53.1106	0.0184	0.1539	0.0000	0.1539	0.9978
026	63.7696	18.4349	45.0840	63.5189	0.0343	**0.0310**	0.0000	**0.0310**	0.9991
335	68.4433	40.3155	27.9238	68.2393	0.0470	0.0390	0.0000	0.0390	0.9983

InAs hkl	θ_0 [°]	τ [°]	ω_0 [°]	$\omega_0+\tau$ [°]	w_ω [°]	w_G [°]	w_L [°]	w_V [°]	R^2
002	14,7326	0.0000	0.2034	0.2034	0.0457	**0.0190**	0.0034	**0.0209**	0.9997
004	30,5717	0.0000	0.3060	0.3060	0.0457	0.0317	0.0100	0.0374	0.9984
115	41,3541	15.793	-15.3754	0.4178	0.0435	0.0651	0.0157	0.0739	0.9982
135	48,7859	32.311	-31.8183	0.4932	0.0426	0.1434	0.0126	0.1503	0.9991
006	49,7226	0.0000	0.4936	0.4936	0.0493	0.0600	0.0242	0.0740	0.9900
335	56,4915	40.315	-39.7000	0.6155	0.0445	0.1435	0.0227	0.1560	0.9971
226	57,5056	25.239	-24.6025	0.6369	0.0494	0.0996	0.0273	0.1150	0.9877

3.5. X-ray diffraction patterns and pure line profiles

To characterize parameters of crystalline microstructure of a material under study, pure line profiles must be analysed. The pure line profile *f* originating from the crystal planes hkl corresponding to the Bragg angle $\theta_{0,hkl}$ can be obtained by solving a convolution integral equation of the first kind:

$$\int_{-u}^{+u} g_{hkl}\ \ s-t\ f_{hkl}\ t\ \ = h_{hkl}(s) \tag{13}$$

where g is the standard (instrumental) profile, h is the experimental profile, *s* is the reciprocal space vector length ($s \simeq 4\pi\lambda^{-1}(\theta-\theta_{0,hkl})\cos\theta_{0,hkl}$), λ is the X-ray wavelength, u is a sufficiently large number to ensure good approximation. Deconvolution is an ill-posed problem and should be regularised [56]. In this work the simplified descriptive regularisation was applied, based on fact that both experimental and standard XRD line profiles were well approximated by Voigt functions. Having experimental and standard line profiles approximately decomposed into Gauss-function and Lorentz-function parts (convolutive multipliers) one can easily found the solution to (13) in the form of a Voigt function. The method is based on the theorem on convolution of two Voigt functions: it is the convolution of Gauss and Lorentz components being convolutions of corresponding components of both convolved functions:

$$f_V = f_{V_1} * f_{V_2} = (f_{G_1} * f_{L_1}) * (f_{G_2} * f_{L_2}) = (f_{G_1} * f_{G_2}) * (f_{L_1} * f_{L_2}) = f_G * f_L, \tag{14}$$

where the widths (FWHM) of component functions satisfy the equalities:

$$w_G^2 = w_{G_1}^2 + w_{G_2}^2 \ \text{ and } w_L = w_{L_1} + w_{L_2}. \tag{15}$$

Deconvolution was performed via decomposing experimental and standard line profiles as Voigt functions (with using Origin software to solving this non-linear least squares problem) and computing pure line profiles as Voigt functions with component widths following from

formula (15):

$$w_G^f = \sqrt{{w_G^h}^{\,2} - (w_G^g)^2} \quad \text{and} \quad w_L^f = w_L^h - w_L^g \,. \tag{16}$$

Since, according to formulae (4-8), only the widths of pure line profiles were further analysed to determine microstructural characteristics, in fact only $w_L^f = w_L^h$, $w_G^f = \sqrt{{w_G^h}^{\,2} - \ 0.01203^{\,2}}$, and then w_V^f from formula (12) were calculated for each line profile. Although the approximate decomposition of a function into Gauss-function and Lorentz-function convolution components from (9) is in general unstable with respect to approximate problem data, only when $w_L^h \geq w_L^g$ and $w_G^h \geq w_G^g$ the solution f to (13) may be found in a stable way through solving (9) for h and g given, computing component widths of f from (16) and finally calculating w_V^f from (12) and f from formula (9) (if needed). In this way both the width w_V^f and the solution f can be found stably while component widths may vary within the same approximation inaccuracy (for example following from measurements) and be unreliable. Any simplified analysis of crystalline microstructure based on immediate exploiting w_G^f and w_L^f computed by this method may be in general unstable and unreliable. In this work only resulting widths of pure line profiles w_V^f are involved in microstructure analysis based on formulae (4-8).

The XRD patterns from indium arsenide specimen are illustrated in Figure 3 (whole diffractogram for central area $0{,}0$ and XRD line profiles of reflexions $002, 004, 006$ for all nine specimen areas). An example of the results of measurements and computations is shown in Table 5 for central area $0{,}0$ and all reflexions analysed. Evidently the instrumental contributions are significant only to two line profiles corresponding to smaller Bragg angles.

Table 5. Simplified deconvolution of pure line profiles f (calculated) from pairs of experimental h and standard g ones (measured) through representing all them as Voigt functions: the widths of Voigt functions w_V together with widths of Gauss-function and Lorentz-function components w_G, w_L approximating XRD line profiles for central area $(0{,}0)$ of indium arsenide specimen (all widths are given in diffraction angle 2θ scale).

hkl	θ_0 [°]	w_G^h [°]	w_L^h [°]	w_V^h [°]	w_G^g [°]	w_L^g [°]	w_V^g [°]	w_G^f [°]	w_L^f [°]	w_V^f [°]
002	14,7326	0.0190	0.0032	0.0207	0.0120	0.0000	0.0120	0.0147	0.0032	0.0164
004	30,5717	0.0322	0.0096	0.0377	0.0120	0.0000	0.0120	0.0299	0.0096	0.0354
115	41,3541	0.0664	0.0150	0.0748	0.0120	0.0000	0.0120	0.0653	0.0150	0.0737
135	48,7859	0.1420	0.0148	0.1501	0.0120	0.0000	0.0120	0.1415	0.0148	0.1496
006	49,7226	0.0555	0.0270	0.0713	0.0120	0.0000	0.0120	0.0542	0.0270	0.0700
335	56,4915	0.1328	0.0261	0.1473	0.0120	0.0000	0.0120	0.1323	0.0261	0.1468
226	57,5056	0.0880	0.0366	0.1092	0.0120	0.0000	0.0120	0.0871	0.0366	0.1084

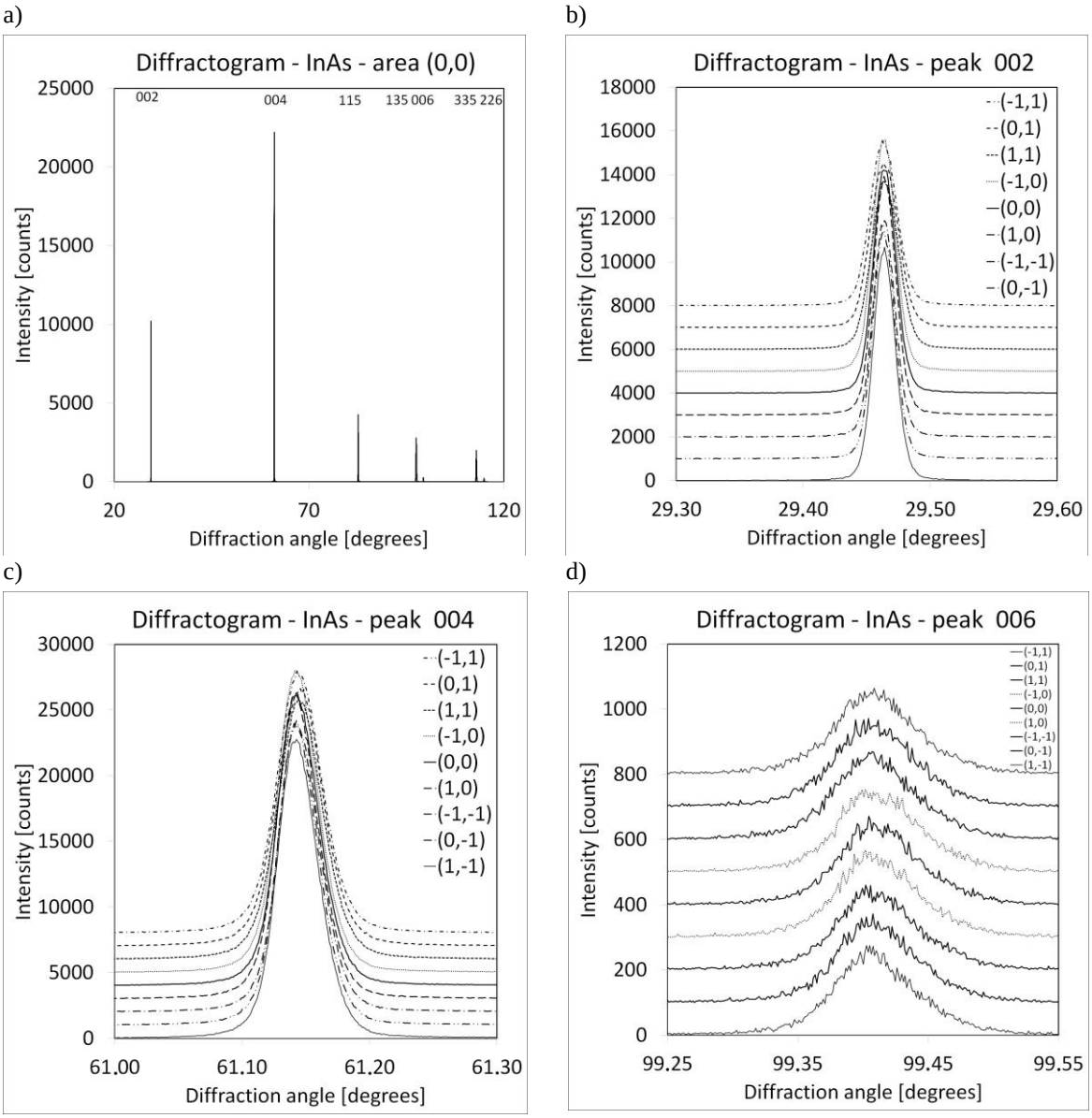

Fig. 3. The XRD patterns recorded from indium arsenide plate specimen: whole for central area $0,0$ (a) and for all nine areas related reflexions 002 ((b), subsequent curves shifted each other by a thousand counts), 004 ((c), subsequent curves shifted each other by a thousand counts) and 006 ((d), subsequent curves shifted each other by a hundred counts).

3.6. Crystalline structure of indium arsenide specimen

The experimental peak positions were together analysed as approximating Bragg angles to find the unit-cell constants from formulae (1-3). Firstly, according to the strong texture in the specimen and well-determined orientation of diffracting planes respectively specimen surface, all line profiles were indexed uniquely with use of approximate value of $a = 0.60580\ \mathrm{nm}$. For each area experimental interplanar distances were determined according to (1) and then with use of (2) the unit-cell constants were determined as minimising functional (3). Since permanent compressive shear stress and resulting strain in plane (001) of the specimen layer was expected, two structures were considered – cubic and tetragonal with $[001]$ axes perpendicular to the specimen surface. Additionally, possible small shift δ of diffraction angle scale (same for all

reflexions) were taken into account. The minimisers of corresponding functionals:

$$a,\delta \ = \arg\min\{\psi^2(\,a,\delta): a>0\} \quad \text{or} \quad a,c,\delta \ = \arg\min\{\psi^2(\,a,c,\delta): a,c>0\} \tag{17}$$

were found by algorithm of approximate optimisation for each specimen area.

The computations were performed in three series. Firstly the unit cell constants were computed for both structures with zero δ assumed. A better approximation were found for tetragonal lattice. Secondly full problem (17) was solved for both structures. For each specimen area the approximation to measured data occurred much better (with much smaller value of (3)) for tetragonal lattice than for cubic one, but with different shift of diffraction angle values. Therefore only results for tetragonal structure were considered to be reliable and hence the computations were repeated only for cubic structure with the same δ as determined for tetragonal one. The resulting root-mean-square relative error (3) was taken as relative error in the determined unit-cell constants; the absolute error was calculated by multiplication. The results for central area $(0,0)$ are collected in Table 6 to illustrating details. The values of unit-cell constants with corresponding error estimates following from minimal values of similarity functional (3, 17) are collected in Table 7. The resulting errors of approximation of model interplanar distances to experimental ones (after correction for shift of diffraction angle scale) are much less for tetragonal lattice than for cubic one, what supports the hypothesis of stress-enforced permanent (first-order) strain and effective (pseudo) tetragonality of the indium arsenide specimen. The unit-cell constant for cubic lattice varies slightly between sample areas; the mean of all nine is $a = 0.606040\ \mathrm{nm}$ with the standard deviation of $0.000010\ \mathrm{nm}$ which is around twelve times less than for each value for single area. The unit-cell constants (especially c) for tetragonal lattice vary slightly in each zone of three vicinal areas:
$[(-1,1),(0,1),(1,1)],\ [(-1,0)\ ,(0,0),(1,0)],[\ (-1,-1),(0,-1),(1,-1)]$, and therefore the means for these three zones (presented in lower part of Table 7) are taken as representative for the specimen, they differ between zones significantly (especially values of c); this time the resulting standard deviations for these triples are similar (for c) or a little larger (for a) as estimates for each sample area. Characteristics of crystalline structure (tetragonal compared with cubic one) of the specimen in these three zones like lattice constants, tetragonality and strains in directions $[100],[010]$ (in plane 001) or $[001]$ and change of unit-cell volume are gathered in Table 8 (with estimates of uncertainties given in Table 7). The compression of around 0.001 in two directions in plane 001 is accompanied by tension of around 0.00015 in perpendicular direction $[001]$ with resulting diminution of unit-cell volume of around -0.002. The tetragonality rations in the three zones are significantly different.
A reliable estimation of shift of diffraction angle scale is important, since set of seven Bragg angles corresponding precisely to a cubic lattice might be falsely interpreted as corresponding precisely to a tetragonal lattice when suitable but false value of δ were admitted.

The method for estimation and quantitative characterisation of tetragonality applied in this work is based on exploiting only diffractograms recorded in standard (for HRXRD) way, differently than in experimental works in which difficult measurements of line profiles from diffracting planes perpendicular to semiconductor plate surface are performed [54, 55].

Table 6. Results of computations of unit-cell constants for area $0,0$ of indium arsenide plate under assumption of tetragonal lattice with [001] axis perpendicular to the layer surface: Bragg (reflexion) angles θ_0 [rad] and interplanar distances d determined from measured XRD peak positions and calculated as solutions to inverse problem, with relative errors; the resulting values are: $\delta = -0.0381$ mrad, $\psi = 0.000021$, $a = 0.605387 \pm 0.000013$ nm, $c = 0.606126 \pm 0.000013$ nm.

h	k	l	$\theta_{0,hkl-m} + \delta$ [rad]	$\theta_{0,hkl-c}$ [rad]	$\frac{\theta_{0-m} - \theta_{0-c}}{\theta_{0-m}}$	d_{hkl-m} [nm]	d_{hkl-c} [nm]	$\frac{d_m - d_c}{d_m}$
0	0	2	0.2569913	0.2570294	0.0001510	0.3030621	0.3030630	-0.0000028
0	0	4	0.5332473	0.5332854	0.0000501	0.1515344	0.1515315	0.0000193
1	1	5	0.7213711	0.7214092	0.0000512	0.1166386	0.1166384	0.0000013
1	3	5	0.8513091	0.8513472	0.0001036	0.1024137	0.1024182	-0.0000439
0	0	6	0.8672021	0.8672401	0.0000589	0.1010199	0.1010210	-0.0000110
3	3	5	0.9858862	0.9859243	0.0000017	0.0923883	0.0923861	0.0000241
2	2	6	1.0031457	1.0031838	0.0000176	0.0913578	0.0913566	0.0000130

Table 7. Results of computations of unit-cell constants for all areas of indium arsenide plate under assumption of tetragonal lattice or cubic lattice (both with [001] axis perpendicular to the layer surface): a, c – unit-cell constants for tetragonal lattice, a_c – unit-cell constant for cubic lattice, s_{at}, s_{ct}, s_{ac} – estimates of absolute errors computed from root-mean-square relative errors ψ_t, ψ_c of estimating interplanar distances (being effectively standard deviations describing dispersion of unit-cell constant values corresponding to measured ones around the computed estimate), δ – shift of diffraction angle scale. Finally, as representative for the investigated sample, three pairs of tetragonal lattice constants and one constant for cubic lattice were taken (boldfaced for zones of areas [$(-1,1), (0,1), (1,1)$], [$(-1,0), (0,0), (1,0)$], [$(-1,-1), (0,-1), (1,-1)$]).

	Tetragonal lattice					Cubic lattice			
Area	a [nm]	s_{at} [nm]	c [nm]	s_{ct} [nm]	ψ_t a, c, δ	a_c [nm]	s_{ac} [nm]	ψ_c a, δ	δ [mrad]
$-1,1$	0.605381	0.000018	0.606155	0.000019	0.000031	0.606048	0.000120	0.000198	-0.170
$0,1$	0.605403	0.000007	0.606152	0.000007	0.000012	0.606049	0.000115	0.000189	-0.176
$1,1$	0.605354	0.000010	0.606165	0.000010	0.000017	0.606053	0.000124	0.000205	-0.194
$-1,0$	0.605378	0.000007	0.606136	0.000007	0.000012	0.606032	0.000116	0.000192	-0.027
$0,0$	0.605387	0.000013	0.606126	0.000013	0.000021	0.606024	0.000114	0.000188	-0.038
$0,1$	0.605347	0.000016	0.606134	0.000016	0.000027	0.606026	0.000122	0.000201	-0.051
$-1,-1$	0.605431	0.000011	0.606139	0.000011	0.000019	0.606041	0.000109	0.000180	-0.066
$0,-1$	0.605405	0.000012	0.606140	0.000012	0.000020	0.606039	0.000113	0.000187	-0.079
$1,-1$	0.605406	0.000017	0.606144	0.000017	0.000028	0.606042	0.000114	0.000189	-0.093
$(*,1)$	**0.605380**	0.000025	**0.606157**	0.000009		0.606050	0.000003		
$(*,0)$	**0.605370**	0.000021	**0.606132**	0.000015		0.606027	0.000004		
$(*,-1)$	**0.605414**	0.000015	**0.606141**	0.000013		0.606041	0.000002		
$(*,*)$	0.605388	0.000027	0.606143	0.000012		**0.606040**	0.000010		

Table 8. Characteristics of crystalline structure of the specimen in three zones observed in experimental data and comparison of unit-cell constants for cubic (symbols with subscript c) and tetragonal systems together with characteristics of tetragonality and strains in directions $[100], [010]$ (in plane 001) or $[001]$ and change of unit-cell volume. The estimates of uncertainties are given in Table 7.

	Crystal lattice constants			Quotients				Strain		
Area	a [nm]	c [nm]	a_c [nm]	a/c	a/a_c	c/a_c	V_t/V_c	001	$[001]$	V
$(*,1)$	0.605380	0.606157	0.606040	1.001284	0.998911	1.000194	0.998017	-0.001089	0.000194	-0.001983
$(*,0)$	0.605370	0.606088	0.606040	1.001258	0.998896	1.000153	0.997945	-0.001104	0.000153	-0.002055
$(*,-1)$	0.605414	0.606050	0.606040	1.001201	0.998968	1.000167	0.998103	-0.001032	0.000167	-0.001897

3.7. Crystalline microstructure of indium arsenide specimen

The widths of pure line profiles for each specimen area were together analysed and interpreted with using formulae (4-7) and (8) under assumption of model polycrystal described in 2.2. The averaged characteristics of crystalline microstructure: mean crystallite size n, shape coefficient κ, mean-absolute second-order strain e and standard deviation σ of crystallite size distribution have been found as the solutions of an inverse problem reduced to non-linear least-squares problem of minimisation of similarity functional (8):

$$n, \kappa, e, \sigma \ = \operatorname{argmin} \{\varphi^2 \ n, \kappa, e, \overline{\sigma} : n, \kappa, e, \overline{\sigma} > 0\} \tag{18}$$

where $\varphi = \varphi(n, \kappa, e, \sigma)$ is a function of arguments n, κ, e, σ defined by formulae (4-8). Solutions were computed with additional restriction that the size of crystallite in direction $[001]$ may not be larger than the plate thickness of $5.15\ \mu\mathrm{m}$. The standard deviation σ for crystallite size distribution occurred very small and did not influenced the results; therefore it was neglected in final calculations. The monodisperse set of crystallites occurred good model for the investigated indium arsenide plate. Moreover, after several numerical experiments the proper value of width of standard line profile (with only Gauss-function component) was fixed to $\theta \ \ 0.105\ \mathrm{mrad}$ (or $2\theta \ \ 0.012031°$) as mean from results of analysing diffractograms from all areas. In some cases an instability with respect to shape coefficient κ was observed. To stabilising computations, the solutions to inverse problem were finally found as minimisers to smoothing functional of special form:

$$n, \kappa, e \ = \operatorname{argmin} \{\varphi^2 \ n, \kappa, e \ + \alpha \bullet \kappa^2 : \ n, \kappa, e > 0\} \tag{19}$$

with constant regularisation parameter $\alpha = 5.35 \bullet 10^{-8}$. Such regularisation produced stable solutions in all cases although in most cases results obtained without regularisation differed negligibly.

The widths of experimental XRD line profiles were determined with relative errors not larger than 4% (mostly 1% to 2%) which influenced resulting discrepancies (8). The relative errors of recovering the widths of pure line profiles from experiment by those following from the best-fitted model of polycrystal are shown in Table 9 and illustrated for area $(0,0)$ in Figure 4 (this is the worst result from all areas); for each area the root-mean-square relative error (8) is given. The relative errors of recovering single line profiles generally vary around 5%, up to 20% in separate cases, especially for very weak peak 226; such error level is typical of XRD data and acceptable.

The averaged microstructure characteristics for all nine areas: n, κ, e, b, h are collected in Table 10; where $b = n \bullet a\ [\mathrm{nm}]$ is the length of base edge (in directions $[100]$ and $[010]$ parallel to plate surface) and $h = n \bullet \kappa \bullet a\ [\mathrm{nm}]$ is the height (in direction $[001]$ perpendicular to plate surface) of the mean cuboidal crystallite and e is the mean-absolute second-order strain. These characteristics, together with unit-cell constants, are also illustrated in Figure 5. These results evidence crystalline heterogeneity of the investigated indium arsenide plate. It can be regarded as a defected monocrystal with dislocations or equivalently as a mosaic bulk polycrystal (one large crystalline grain) comprising crystallites slightly misoriented each other and separated with only small-angle boundaries in-between. The crystallites are, on average, rode-like and elongated in direction perpendicular to the plate surface. Evidently the mean crystallite sizes (together with shape) and seconds-order strains change from one side of the plate to the opposite one: roughly in the first zone $[\ -1{,}1\ ,\ 0{,}1\ ,\ 1{,}1\ ]$ b~90 nm, h~500 nm ~ $\frac{1}{10}t$, $e \sim 0.000163$, in the second zone $[\ -1{,}0\ ,\ 0{,}0\ ,\ 1{,}0\ ]$ b~60 nm, h~1600 nm ~$\frac{1}{3}t$,

$e \sim 0.000167$, in the third zone $[\,-1,-1\ ,\ 0,-1\ ,\ 1,-1\,]$ b~80 nm, h~5000 nm $\sim t$, e~ 0.000174, (where $t = 5.15\ \mu\mathrm{m}$ is the plate thickness). The mean-absolute second-order strain is small in whole specimen and varies slightly between 0.000159 and 0.000176 being a little smaller in areas with smaller crystallites; nevertheless the contribution from strain into XRD line profiles is significant as it is illustrated in Table 11 for area (0,0) according to formulae (4-7). Each small-angle boundary between side faces of vicinal crystallites may be interpreted as a single dislocation; under such hypothesis for cuboidal crystallites the dislocation density can be calculated as $\rho = 2 \bullet b^{-2}$ – these estimates are given in the last column of Table 10.

The estimation of uncertainties in the computed values of microstructural characteristics are difficult because the inverse problem of determining them is unstable. It can be effectively performed via numerical tests for a specific algorithm and data type (particularly as those considered in this work). To make it, a series of numerical experiments was made. The experimental data from area $(-1,1)$ – widths of Gauss-function and Lorentz-function components of pure line profiles – were perturbed randomly on the similar (although a little excessive) level as difference between model and experimental widths. Then microstructural characteristics were computed by the same algorithm and eventually the mean and standard deviation for the whole sequence of resulting values were calculated for each microstructural parameter. The rounding of the quotient of a standard deviation divided by a mean serves as estimate of relative error in corresponding parameter value. They are: 10% for b, 30% for h, 7% for e; details are shown in Table 12. The mean values from ten-element sequences of experiments agree very well with those obtained from experimental data.

Table 9. Widths (FWHM) [milliradians of reflexion θ angle] of pure line profiles f calculated from pairs of experimental h and standard g ones (measured) through representing all them as Voigt functions and widths calculated for model of microstructure producing the best approximation to whole set of widths for each specimen area separately, with relative errors of recovering; the root-mean-square error of this approximation is shown on the right to each symbol of area; the unit-cell constants for each three-area zone are also displayed.

a [nm]	0.605380		(-1,1)	0.0421		(0,1)	0.0724		(1,1)	0.0647
c [nm]	0.606157	Experiment	Model	Difference	Experiment t	Model	Difference	Experiment	Model	Difference
hkl	θ_0 [rad]	w_V^f [mrad]	w_V^f [mrad]	(relative)	w_V^f [mrad]	w_V^f [mrad]	(relative)	w_V^f [mrad]	w_V^f [mrad]	(relative)
002	0.256977	0.184	0.184	-0.001	0.195	0.198	0.012	0.189	0.192	0.012
004	0.533228	0.340	0.342	0.004	0.349	0.344	-0.016	0.341	0.334	-0.020
115	0.721331	0.576	0.532	-0.083	0.591	0.547	-0.082	0.572	0.543	-0.054
135	0.851221	0.839	0.817	-0.027	0.956	0.888	-0.077	0.973	0.902	-0.079
006	0.867129	0.621	0.647	0.040	0.634	0.639	0.007	0.623	0.622	-0.002
335	0.985885	1.025	1.077	0.048	1.115	1.169	0.046	1.144	1.188	0.037
226	1.003104	0.946	0.977	0.031	0.867	1.016	0.146	0.879	1.017	0.135

a [nm]	0.605370		(-1.0)	0.0945		(0.0)	0.1125		(1.0)	0.1105
c [nm]	0.606132	Experiment t	Model	Difference	Experiment	Model	Difference	Experiment t	Model	Difference
hkl	θ_0 [rad]	w_V^f [mrad]	w_V^f [mrad]	(relative)	w_V^f [mrad]	w_V^f [mrad]	(relative)	w_V^f [mrad]	w_V^f [mrad]	(relative)
002	0.256988	0.145	0.146	0.006	0.143	0.145	0.010	0.141	0.143	0.009
004	0.533253	0.306	0.310	0.014	0.309	0.306	-0.008	0.306	0.305	-0.003
115	0.721366	0.635	0.616	-0.030	0.643	0.606	-0.061	0.657	0.622	-0.056
135	0.851260	1.307	1.138	-0.148	1.305	1.120	-0.165	1.361	1.166	-0.167
006	0.867177	0.635	0.609	-0.044	0.611	0.600	-0.019	0.614	0.600	-0.024
335	0.985931	1.357	1.502	0.097	1.281	1.478	0.133	1.327	1.539	0.138
226	1.003161	0.997	1.199	0.168	0.946	1.179	0.198	0.988	1.216	0.187

a [nm]	0.605414		(-1.-1)	0.0764		(0.-1)	0.0781		(1.-1)	0.0793
c [nm]	0.606141	Experiment t	Model	Difference	Experiment t	Model	Difference	Experiment t	Model	Difference
hkl	θ_0 [rad]	w_V^f [mrad]	w_V^f [mrad]	(relative)	w_V^f [mrad]	w_V^f [mrad]	(relative)	w_V^f [mrad]	w_V^f [mrad]	(relative)
002	0.256984	0.140	0.141	0.003	0.139	0.139	0.003	0.138	0.139	0.007
004	0.533244	0.307	0.311	0.015	0.303	0.308	0.016	0.306	0.308	0.007
115	0.721349	0.622	0.566	-0.098	0.617	0.561	-0.099	0.621	0.565	-0.100
135	0.851224	1.025	0.941	-0.089	1.018	0.936	-0.088	1.038	0.949	-0.095
006	0.867160	0.619	0.618	-0.002	0.615	0.611	-0.006	0.609	0.611	0.003
335	0.985872	1.135	1.243	0.087	1.138	1.236	0.079	1.133	1.253	0.096
226	1.003121	0.938	1.071	0.125	0.918	1.063	0.137	0.938	1.072	0.126

Table 10. Averaged microstructural characteristics of indium arsenide specimen in centres of square areas: b [nm] is length of square base edge and h [nm] is height of the mean crystallite and e is the mean-absolute second-order strain; the estimate of dislocation density ρ from size b of the mean crystallite is added.

Area	n	κ	$b = n \bullet a$ [nm]	h	e	$\varphi(n, \kappa, e)$	ρ [m^{-2}]
(-1,1)	177.8	5.52	107.7	595	0.000169	0.0421	$1.73 \bullet 10^{14}$
(0,1)	143.7	5.59	87.0	487	0.000163	0.0724	$2.64 \bullet 10^{14}$
(1,1)	136.9	6.09	82.9	505	0.000159	0.0647	$2.91 \bullet 10^{14}$
(-1,0)	96.5	27.7	58.4	1618	0.000169	0.0945	$5.86 \bullet 10^{14}$
(0,0)	98.1	25.2	59.4	1499	0.000166	0.1125	$5.67 \bullet 10^{14}$
(1,0)	92.9	31.6	56.2	1777	0.000167	0.1105	$6.33 \bullet 10^{14}$
(-1,-1)	131.8	59.8	79.8	4778	0.000176	0.0764	$3.14 \bullet 10^{14}$
(0,-1)	132.0	57.3	79.9	4585	0.000174	0.0781	$3.13 \bullet 10^{14}$
(1,-1)	128.9	66.0	78.0	5154	0.000174	0.0793	$3.28 \bullet 10^{14}$

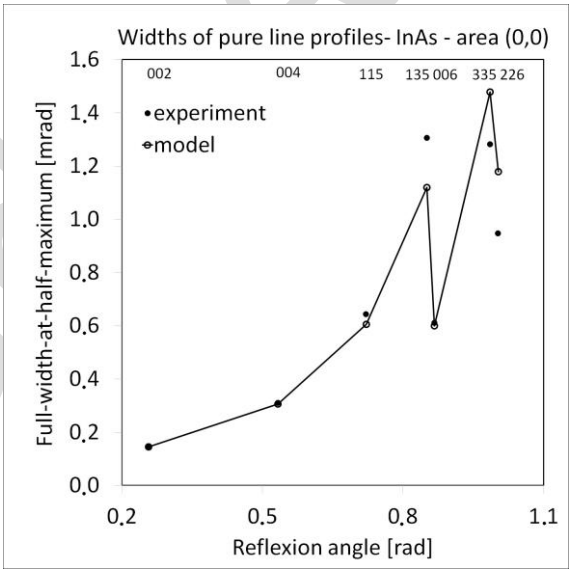

Fig. 4. Widths (FWHM) [milliradians of reflexion angle] of pure line profiles f calculated from pairs of experimental h and standard g ones (measured) through representing all them as Voigt functions and widths calculated for model of microstructure producing the best approximation to whole set of widths for $0{,}0$ specimen area (polygonal chain is added only for better visibility of sequence of model values).

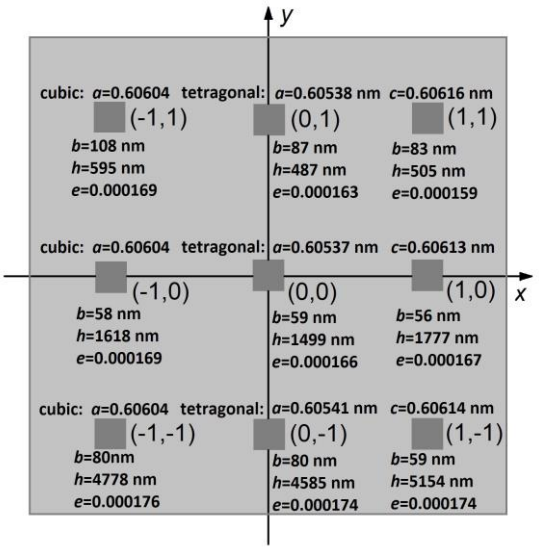

Fig. 5. Averaged microstructural characteristics and unit-cell parameters (for permanent cubic lattice and for enforced by stress from substrate pseudo-tetragonal lattice) of indium arsenide specimen in centres of square areas: b [nm] is length of square base edge (in plane (001)) and h [nm] is height (in direction [001]) of the mean crystallite and e is mean-absolute second-order strain.

Table 11. Widths (FWHM) [milliradians of reflexion angle] of pure line profiles f calculated from pairs of experimental h and standard g ones (measured) through representing all them as Voigt functions and widths calculated for model of microstructure producing the best approximation to whole set of widths for area (0,0); widths of hypothetical line profiles from crystallite shape and sizes and from second-order strain contributing (as convolutive multipliers) into model pure line profiles are also presented.

InAs area (0,0)		Model	Model	Model	Experiment	Difference
hkl	θ_0 [rad]	$w_{f,k}$ [mrad]	$w_{f,r}$ [mrad]	w_f [mrad]	w_V^f [mrad]	(relative)
002	0.256988	0.048	0.129	0.145	0.143	0.010
004	0.533253	0.054	0.290	0.306	0.309	-0.008
115	0.721366	0.402	0.432	0.606	0.643	-0.061
135	0.851260	0.968	0.560	1.120	1.305	-0.165
006	0.867177	0.072	0.579	0.600	0.611	-0.019
335	0.985931	1.276	0.742	1.478	1.281	0.133
226	1.003161	0.870	0.770	1.179	0.946	0.198

3.8. Heterogeneity of crystalline state of investigated indium arsenide specimen

The investigated thin plate of pure indium arsenide is a mosaic monocrystal with non-homogeneous crystalline microstructure and deformed crystalline structure. Three zones of three areas with similar characteristics are observed; for emphasising the similarities and differences between zones rough estimates of principal parameters are shown in Table 13.

Another property of specimen is visible in values of shift δ of diffraction angle scale. The dependence of δ on experimental conditions (especially configuration of a diffractometer) is generally complex [58] but for a HR HRD diffractometer with almost-parallel well collimated and almost-monochromatic X-ray beam it is principally effect of specimen displacement bellow ($\delta < 0$) or up ($\delta > 0$ – toward X-ray tube) rotation axis at the stage sample level. The specimen plate is bend along central zone (central horizontal line at diagrams in Figure 1 and Figure 5) and convex toward X-ray tube and detector. This bend to some extent can be caused by interaction of gallium arsenide substrate with indium arsenide cover layer; the detailed analysis of stresses in the whole specimen is beyond the scope of this work.

Table 12. Averaged microstructural characteristics of indium arsenide specimen in central square area calculated from widths of Gaussian and Lorentzian components of line profiles from measurements (0) and simulated (1-10) by adding to them random disturbances with resulting root-mean-square relative error around 0.05 (two last columns): b [nm] is length of square base edge and h [nm] is height of the mean crystallite and e is mean-absolute second-order strain; artificial data differ to those from measurements at the same level as the measured and modelled ones; the standard deviation (S) and relative standard deviation (R) corresponding to series mean (M) are estimates of errors in corresponding parameters.

−1,1	n	κ	$b = n \bullet a$ [nm]	$h = n \bullet \kappa \bullet a$ [nm]	e	$\varphi(n,\kappa,e)$	w_L^f	w_G^f
0	177.6	5.52	107.6	594.7	0.000169	0.0421	0	0
1	184.7	5.29	111.9	592.3	0.000171	0.0463	0.0438	0.0317
2	146.0	5.30	88.4	468.6	0.000149	0.0443	0.0556	0.0413
3	194.2	5.45	117.6	641.7	0.000173	0.0645	0.0545	0.0437
4	172.3	4.63	104.3	482.8	0.000169	0.0322	0.0398	0.0465
5	189.6	8.09	114.8	929.2	0.000183	0.0540	0.0508	0.0338
6	160.0	4.74	96.9	459.7	0.000161	0.0550	0.0472	0.0359
7	195.3	6.89	118.3	815.3	0.000176	0.0168	0.0446	0.0536
8	156.4	4.92	94.7	466.2	0.000157	0.0858	0.0625	0.0489
9	180.6	5.84	109.4	639.5	0.000170	0.0164	0.0390	0.0590
10	156.8	4.52	94.9	429.0	0.000153	0.0439	0.0510	0.0602
M	**174.0**	**5.56**	**105.3**	**592.6**	**0.000166**	**0.0456**	**0.0444**	**0.0413**
S	**16.9**	**1.07**	**10.3**	**159.8**	**0.000010**	**0.0200**	**0.0163**	**0.0167**
R	**0.097**	**0.192**	**0.097**	**0.270**	**0.062**	**0.439**	**0.368**	**0.405**
R	**10%**	**20%**	**10%**	**30%**	**7%**			

Table 13. Structural and averaged microstructural characteristics of indium arsenide specimen in three zones (means from three areas in each zone): [−1,1 , 0,1 , 1,1], [−1,0 , 0,0 , 1,0], [−1, −1 , 0, −1 , 1, −1]; symbols in headers as in Table 8 and Table 10; for cubic lattice the permanent parameter is $a_c = 0.60604$ nm.

Zone	a [nm]	c [nm]	$\frac{a}{c}$	$\frac{a_t}{a_c}$	$\frac{c_t}{a_c}$	$\frac{V_t}{V_c} - 1$	b [nm]	h [nm]	e [%]	ρ [m^{-2}]	δ [mrad]
1	0.60538	0.60616	1.00128	0.99891	1.00019	-0.00198	93	530	0.0169	$2.4 \bullet 10^{14}$	0.177
2	0.60537	0.60609	1.00126	0.99890	1.00015	-0.00206	58	1630	0.0168	$6.0 \bullet 10^{14}$	0.039
3	0.60541	0.60605	1.00120	0.99897	1.00017	-0.00190	79	4840	0.0175	$3.2 \bullet 10^{14}$	0.079

4. Conclusions

In this work the crystalline homogeneity of an undoped indium arsenide epitaxial layer deposited on gallium arsenide substrate by molecular beam epitaxy was studied with using high-resolution X-ray diffraction technique and mathematical modelling of both crystalline structure and crystalline microstructure based on analysing X-ray diffraction patterns. The goals were both elaborating and testing whole procedure for investigating similar materials (including experiment, modelling and computations) and studying the objective specimen.

The specimen was a $20\ \text{mm} \times 20\ \text{mm} \times 5.15\ \mu\text{m}$ plate at which regular 3×3 point grid was plotted to selecting areas of exploration by high-resolution X-ray diffractometry. For each area (of size determined by section of X-ray beam) an XRD pattern containing seven peaks was recorded together with corresponding rocking characteristics. The full-widths-at-half-maximum of the rocking curves for all measurement points and all reflexions were close each other and small, what evidenced high structural homogeneity of the sample with low degree of disorientation of crystallites and strong texture. It was realised that whole plate might be regarded as one mosaic polycrystalline grain as an equivalent to a defected monocrystal containing dislocations. The $(2\theta - \omega)$ XRD line profiles for each specimen area were recorded and explored to determine the averaged parameters of crystal structure – unit-cell constants and

crystal microstructure – mean size and shape of crystallites and mean-absolute second-order deformation of crystalline lattice. The last exploration was based on simplified mathematical model of the crystalline microstructure.

The unit-cell parameter were determined by exploring diffraction peak positions for permanent cubic structure and for pseudo-tetragonal structure enforced by interaction with substrate. The state of permanent (first-order) strain was recognised in whole specimen.

The unit-cell constant of cubic crystal lattice of pure indium arsenide was determined to be $0.606040 \ \pm 0.000010 \ \mathrm{nm}$.

The analysis of XRD data showed that the specimen (approximately) comprised elongated rode-like cuboidal crystallites with square base of edge-lengths of around $90 - 60 - 80 \ \mathrm{nm}$ (parallelly to the surface) and height of around $500 - 160 - 5000 \ \mathrm{nm}$ (perpendicularly to the surface) in three three-area zones (as defined by measurement point grid). In all areas the mean-absolute second-order strain occurred very small of around 0.000170, although contributing to XRD line profiles significantly.

Both structural and microstructural parameters occurred changing from one edge of the square sample plate to the opposite one and being close to constant in parallel zones elongated in perpendicular direction. The plate itself occurred bent along the central axis parallel to zone longer limits.

In this way a new complete procedure to investigating thin semiconductor plates (epitaxial layers), including HRXRD measurements with mathematical structure and microstructure modelling combined with computations, was proposed and successfully applied to determine both the structural and microstructural characteristics of such specimen.

Acknowledgements

This work has been completed with the financial support under the program of the Polish Ministry of Education and Science: “Regional Initiative of Excellence” in 2019-2023, project No. 014/RID/2018/19, funding amount of 4 589 200 PLN.

References

[1] Vurgaftman, I., Meyer, J. R., & Ram-Mohan, L. R. (2001). Band parameters for III–V compound semiconductors and their alloys. *Journal of Applied Physics*, *89*(11), 5815–5875. https://doi.org/10.1063/1.1368156

[2] Kroemer, H. (2004). The family (InAs, GaSb, AlSb) and its heterostructures: a selective review. *Physica E: Low-dimensional Systems and Nanostructures*, *20*(3–4), 196–203. https://doi.org/10.1016/j.physe.2003.08.003

[3] Wang, F., Chen, J., Xu, Z., Zhou, Y., Xu, Q., & Li, H. (2014). Molecular beam epitaxy growth of high quality InAs/GaSb type-II superlattices for long wavelength infrared detection. *Proceedings of SPIE*. https://doi.org/10.1117/12.2068276

[4] Rogalski, A., Kopytko, M., & Martyniuk, P. (2018). *Antimonide-based Infrared Detectors: A New Perspective*. SPIE Press. https://doi.org/10.1117/3.2278814

[5] Nie, B., Huang, J., Zhao, C., Zhang, Y., & Ma, W. (2020). Long wavelength Type II INAS/GASB Superlattice photodetector using resonant tunneling diode structure. *IEEE Electron Device Letters*, *41*(1), 73–75. https://doi.org/10.1109/led.2019.2953896

[6] Zhylik, A., Benediktovich, A., Ulyanenkov, A., Guérault, H., Myronov, M., Dobbie, A., Leadley, D. R., & Ulyanenkova, T. (2011). High-resolution x-ray diffraction investigation of relaxation and dislocations in SiGe layers grown on (001), (011), and (111) Si substrates. *Journal of Applied Physics*, *109*(12). https://doi.org/10.1063/1.3597828

[7] Hédi, F., Mohamed Mourad, H., & Ahmed, R. (2017). High-Resolution X-Ray Diffraction of III–V Semiconductor Thin Films. In A. Alicia Esther (Ed.), *X-ray Scattering*. IntechOpen. https://doi.org/10.5772/65404

[8] Bismayer, U., Brinksmeier, E., Güttler, B., Seibt, H., & Menz, C. (1994). Measurement of subsurface damage in silicon wafers. *Precision Engineering*, *16*(2), 139–144. https://doi.org/10.1016/0141-6359(94)90199-6

[9] Herms, M., Fukuzawa, M., Melov, V. G., Schreiber, J., Möck, P., & Yamada, M. (2000). Residual strain in annealed GaAs single-crystal wafers as determined by scanning infrared polariscopy, x-ray diffraction and topography. *Journal of Crystal Growth*, *210*(1–3), 172–176. https://doi.org/10.1016/s0022-0248(99)00673-9

[10] Alaydin, B. O., Tuzemen, E. S., Altun, D., & Elagoz, S. (2019). Comprehensive structural and optical characterization of AlAs/GaAs distributed bragg reflector. *International Journal of Modern Physics B*, *33*(08), 1950054. https://doi.org/10.1142/s0217979219500541

[11] Ataser, T., Demir, D., Bilgili, A. K., Ozturk, M., & Ozcelik, S. (2021). Mosaic Defects of AlN Buffer Layers in GaN/AlN/4H-SiC Epitaxial Structure. *Journal of Polytechnic*, *24*(2), 511–516. https://doi.org/10.2339/politeknik.682649

[12] Benyahia, D., Kubiszyn, Ł., Michalczewski, K., Boguski, J., Kębłowski, A., Martyniuk, P., Piotrowski, J., & Rogalski, A. (2018). Electrical properties of midwave and longwave InAs/GaSb superlattices grown on GaAs substrates by molecular beam epitaxy. *Nanoscale Research Letters*, *13*(1). https://doi.org/10.1186/s11671-018-2612-4

[13] Michalczewski, K., Jureńczyk, J., Kubiszyn, Ł., & Martyniuk, P. (2022). The dependence of InAs/InAsSb superlattice detectors' spectral response on molecular beam epitaxy growth temperature. *Applied Sciences*, *12*(3), 1368. https://doi.org/10.3390/app12031368

[14] Kojdecki, M. A., Ruiz de Sola, E., Serrano, F. J., Delgado-Pinar, E., Reventós, M. M., Esteve, V. J., Amigó, J. M., & Alarcón, J. (2007). Microstructural evolution of mullites produced from single-phase gels. *Journal of Applied Crystallography*, *40*(2), 260–276. https://doi.org/10.1107/s0021889807000295

[15] Kojdecki, M. A., Ruiz de Sola, E., Serrano, F. J., Amigó, J. M., & Alarcón, J. (2009). Comparative x-ray diffraction study of the crystalline microstructure of tetragonal and monoclinic vanadium–zirconium dioxide solid solutions produced from gel precursors. *Journal of Applied Crystallography*, *42*(2), 198–210. https://doi.org/10.1107/s0021889809005135

[16] Kojdecki, M. A., Bastida, J., Pardo, P., & Amorós, P. (2005). Crystalline microstructure of sepiolite influenced by grinding. *Journal of Applied Crystallography*, *38*(6), 888–899. https://doi.org/10.1107/s0021889805026476

[17] Serrano, F. J., Montoya, N., Pizarro, J. L., Reventós, M. M., Kojdecki, M. A., Amigó, J. M., & Alarcón, J. (2013). Crystal structure and microstructure of synthetic hexagonal magnesium–cobalt cordierite solid solutions (Mg2−2xCo2xAl4Si5O18). *Acta Crystallographica Section B Structural Science, Crystal Engineering and Materials*, *69*(2), 110–121. https://doi.org/10.1107/s2052519213001401

[18] Pardo, P., Kojdecki, M. A., Calatayud, J. M., Amigó, J. M., & Alarcón, J. (2017). Crystalline microstructure of boehmites studied by multi-peak analysis of powder X-ray diffraction patterns. *Powder Diffraction*, *32*(S1), S87–S98. https://doi.org/10.1017/s0885715617000641

[19] Williamson, G. K., & Hall, W. H. (1953). X-ray line broadening from filed aluminium and wolfram. *Acta Metallurgica*, *1*(1), 22–31. https://doi.org/10.1016/0001-6160(53)90006-6

[20] Izumi, F., & Ikeda, T. (2014). Implementation of the Williamson-Hall and Halder-Wagner Methods into RIETAN-FP.

[21] Prabhu, Y. T., Rao, K. V., Kumar, V. S. S., & Kumari, B. S. (2014). X-Ray Analysis by Williamson-Hall and Size-Strain Plot Methods of ZnO Nanoparticles with Fuel Variation. *World Journal of Nano Science and Engineering*, *04*(01), 21–28. https://doi.org/10.4236/wjnse.2014.41004

[22] Egorov, I. N., Egorova, S. I., & Ya Egorov, N. (2020). X-ray Diffraction Analysis by Williamson-Hall Method of Strontium Hexaferrite Lattice Features after Mechanical Milling. *IOP Conference Series: Materials Science and Engineering*, *969*(1), 012006. https://doi.org/10.1088/1757-899x/969/1/012006

[23] Jabir, S. A.-A., & Harbbi, K. H. (2020). A comparative study of Williamson-Hall method and size-strain method through X-ray diffraction pattern of cadmium oxide nanoparticle. *AIP Conference Proceedings*. https://doi.org/10.1063/5.0033762

[24] Magalhães, S., Cabaço, J. S., Mateus, R., Faye, D. Nd., Pereira, D. R., Peres, M., Lorenz, K., Díaz-Guerra, C., Araújo, J. P., & Alves, E. (2021). Crystal mosaicity determined by a novel layer deconvolution Williamson–Hall method. *CrystEngComm*, *23*(10), 2048–2062. https://doi.org/10.1039/d0ce01669a

[25] Warren, B. E., & Averbach, B. L. (1950). The Effect of Cold-Work Distortion on X-Ray Patterns. *Journal of Applied Physics*, *21*(6), 595–599. https://doi.org/10.1063/1.1699713

[26] Turunen, M. J., Keijser, Th. de, Delhez, R., & Pers, N. M. van. der. (1983). A method for the interpretation of the Warren–Averbach mean-squared strains and its application to recovery in aluminium. *Journal of Applied Crystallography*, *16*(2), 176–182. https://doi.org/10.1107/s0021889883010225

[27] Bourniquel, B., Sprauel, J. M., Feron, J., & Lebrun, J. L. (1989). Warren-Averbach Analysis of X-ray Line Profile (even truncated) Assuming a Voigt -like Profile. In G. Beck, S. Denis & A. Simon (Eds.), *International Conference on Residual Stresses: ICRS2* (pp. 184-189). Springer Netherlands. https://doi.org/10.1007/978-94-009-1143-7_29

[28] Drits, V. A., Eberl, D. D., & Środoń, J. (1998). XRD Measurement of Mean Thickness, Thickness Distribution and Strain for Illite and Illite-Smectite Crystallites by the Bertaut-Warren-Averbach Technique. *Clays and Clay Minerals*, *46*(1), 38–50. https://doi.org/10.1346/ccmn.1998.0460105

[29] Marinkovic, B., Avillez, R. R. de, Saavedra, A., & Assunção, F. C. R. (2001). A comparison between the Warren-Averbach method and alternate methods for X-ray diffraction microstructure analysis of polycrystalline specimens. *Materials Research*, *4*(2), 71–76. https://doi.org/10.1590/s1516-14392001000200005

[30] Ichikawa, R. U., Martinez, L. G., Imakuma, K., & Turrillas, X. (2014, September). Development of a methodology for the application of the Warren-Averbach method. *Anais Do v Encontro Científico de Física Aplicada*. https://doi.org/10.5151/phypro-ecfa-049

[31] Sanz, A., Bastida, J., Caballero, A., & Kojdecki, M. (2018). X-ray diffraction Warren–Averbach mullite analysis in whiteware porcelains: influence of kaolin raw material. *Clay Minerals*, *53*(3), 471–485. https://doi.org/10.1180/clm.2018.34

[32] Balzar, D. (1992). Profile fitting of X-ray diffraction lines and Fourier analysis of broadening. *Journal of Applied Crystallography*, *25*(5), 559–570. https://doi.org/10.1107/s0021889892004084

[33] Vargas, R., Louër, D., & Langford, J. I. (1983). Diffraction line profiles and Scherrer constants for materials with hexagonal crystallites. *Journal of Applied Crystallography*, *16*(5), 512–518. https://doi.org/10.1107/s0021889883010924

[34] Langford, J. I., Boultif, A., Auffrédic, J. P., & Louër, D. (1993). The use of pattern decomposition to study the combined X-ray diffraction effects of crystallite size and stacking faults in ex-oxalate zinc oxide. *Journal of Applied Crystallography*, *26*(1), 22–33. https://doi.org/10.1107/s0021889892007684

[35] Langford, J. I., Louër, D., & Scardi, P. (2000). Effect of a crystallite size distribution on X-ray diffraction line profiles and whole-powder-pattern fitting. *Journal of Applied Crystallography*, *33*(3), 964–974. https://doi.org/10.1107/s002188980000460x

[36] Ungár, T., Dragomir-Cernatescu, I., Louër, D., & Audebrand, N. (2001). Dislocations and crystallite size distribution in nanocrystalline CeO2 obtained from an ammonium cerium(IV)-nitrate solution. *Journal of Physics and Chemistry of Solids*, *62*(11), 1935–1941. https://doi.org/10.1016/s0022-3697(01)00029-4

[37] Leoni, M., & Scardi, P. (2004). Nanocrystalline domain size distributions from powder diffraction data. *Journal of Applied Crystallography*, *37*(4), 629–634. https://doi.org/10.1107/s0021889804013366

[38] Scardi, P., & Leoni, M. (2004). Whole Powder Pattern Modelling: Theory and Applications. In E. J. Mittemeijer & P. Scardi (Eds.), *Diffraction Analysis of the Microstructure of Materials* (pp. 51-91). Springer Berlin Heidelberg. https://doi.org/10.1007/978-3-662-06723-9_3

[39] Scardi, P., & Leoni, M. (2006). Line profile analysis: pattern modellingversusprofile fitting. *Journal of Applied Crystallography*, *39*(1), 24–31. https://doi.org/10.1107/s0021889805032978

[40] Scardi, P., Azanza Ricardo, C. L., Perez-Demydenko, C., & Coelho, A. A. (2018). Whole powder pattern modelling macros for TOPAS. *Journal of Applied Crystallography*, *51*(6), 1752–1765. https://doi.org/10.1107/s160057671801289x

[41] Ahmoum, H., Sukor Su'ait, M., Ataollahi, N., Ubaidah Syafiq Mustaffa, M., Boughrara, M., Chelvanathan, P., Sopian, K., Li, G., Kerouad, M., Scardi, P., & Wang, Q. (2021). Suppressing the secondary phases via N2

preheating of Cu2ZnSnS4 thin films with the addition of oleylamine and/or 1-Dodecanethiol solvents. *Inorganic Chemistry Communications*, *134*, 109031. https://doi.org/10.1016/j.inoche.2021.109031

[42] Cervellino, A., Giannini, C., Guagliardi, A., & Ladisa, M. (2005). Nanoparticle size distribution estimation by a full-pattern powder diffraction analysis. *Physical Review B*, *72*(3). https://doi.org/10.1103/physrevb.72.035412

[43] Giannini, C., Guagliardi, A., Zanchet, D., Cervellino, A., & Ladisa, M. (2005). X-ray powder diffraction characterization of nanoparticles. *Acta Crystallographica Section A Foundations of Crystallography*, *61*(a1), c405–c405. https://doi.org/10.1107/s0108767305082814

[44] Cernuto, G., Masciocchi, N., Cervellino, A., Colonna, G. M., & Guagliardi, A. (2011). Size and Shape Dependence of the Photocatalytic Activity of TiO2 Nanocrystals: A Total Scattering Debye Function Study. *Journal of the American Chemical Society*, *133*(9), 3114–3119. https://doi.org/10.1021/ja110225n

[45] Delgado-López, J. M., Frison, R., Cervellino, A., Gómez-Morales, J., Guagliardi, A., & Masciocchi, N. (2013). Crystal Size, Morphology, and Growth Mechanism in Bio-Inspired Apatite Nanocrystals. *Advanced Functional Materials*, *24*(8), 1090–1099. https://doi.org/10.1002/adfm.201302075

[46] Benyahia, D., Kubiszyn, Ł., Michalczewski, K., Kębłowski, A., Martyniuk, P., Piotrowski, J., & Rogalski, A. (2016). Molecular beam epitaxial growth and characterization of InAs layers on GaAs (001) substrate. *Optical and Quantum Electronics*, *48*(9). https://doi.org/10.1007/s11082-016-0698-4

[47] Wróbel, J., Grodecki, K., Benyahia, D., Boguski, J., Murawski, K., Michalczewski, K., Grzonka, J., Umana-Membreno, G., Kubiszyn, Ł., Kębłowski, A., Michałowski, P. P. P., Gomółka, E., Martyniuk, P., Piotrowski, J., Rogalski, A., & Gorczyca, K. (2018). Structural and optical characterization of the high quality Be-doped InAs epitaxial layer grown on GaAs substrate. In P. Struk & T. Pustelny (Eds.), *13th Conference on Integrated Optics: Sensors, Sensing Structures, and Methods*. SPIE. https://doi.org/10.1117/12.2503624

[48] Kojdecki, M. A. (2004). Approximate Estimation of Contributions to Pure X-Ray Diffraction Line Profiles from Crystallite Shapes, Sizes and Strains by Analysing Peak Widths. *Materials Science Forum*, *443–444*, 107–110. https://doi.org/10.4028/www.scientific.net/msf.443-444.107

[49] Kojdecki, M.A., Mielcarek, W., Prociów, K., & Warycha, J. (2009). Comparison of two standards for powder X-ray diffractometry. *Zeitschrift für Kristallographie, Supplement 30*, 183-188. https://doi.org/10.1524/9783486992588-030

[50] Windover, D., Gil, D. L., Henins, A., & Cline, J. P. (2009). D-57 NIST SRM 2000—A High Resolution X-ray Diffraction Standard Reference Material. *Powder Diffraction*, *24*(2), 171–171. https://doi.org/10.1154/1.3176002

[51] Kaiser, D. L., & Watters, R. (2012). Certificate of Analysis - Standard Reference Material 2000 - Calibration Standard for High-Resolution X-Ray Diffraction. *National Institute of Standards & Technology*, Gaithesburg, MD 20889.

[52] Deutsch, M., & Hart M. (1982). Wavelength energy shape and structure of the Cu Kα_1 X-ray emission line. *Physical Review B*, *26*(10), 5558–5567. https://doi.org/10.1103/physrevb.26.5558

[53] Härtwig, J., Hölzer, G., Wolf, J., & Förster, E. (1993). Remeasurement of the profile of the characteristic Cu*K*α emission line with high precision and accuracy. *Journal of Applied Crystallography*, *26*(4), 539–548. https://doi.org/10.1107/s0021889893000160

[54] Serafinczuk, J., Pawlaczyk, L., Moszak, K., Pucicki, D., Kudrawiec, R., & Hommel, D. (2022). X-ray diffraction studies of residual strain in AlN/sapphire templates. *Measurement*, *200*, 111611. https://doi.org/10.1016/j.measurement.2022.111611

[55] Serafińczuk, J., Moszak, K., Pawlaczyk, Ł., Olszewski, W., Pucicki, D., Kudrawiec, R., & Hommel, D. (2020). Determination of dislocation density in GaN/sapphire layers using XRD measurements carried out from the edge of the sample. *Journal of Alloys and Compounds*, *825*, 153838. https://doi.org/10.1016/j.jallcom.2020.153838

[56] Massidda, S., Continenza, A., Freeman, A. J., de Pascale, T. M., Meloni, F., & Serra, M. (1990). Structural and electronic properties of narrow-band-gap semiconductors: InP, InAs, and InSb. *Physical Review B*, *41*(17), 12079–12085. https://doi.org/10.1103/physrevb.41.12079

[57] Kojdecki, M. A. (2001). Deconvolution by Example - Computational Test of Effective Algorithms. *Materials Science Forum*, *378–381*, 12–17. https://doi.org/10.4028/www.scientific.net/msf.378-381.12

[58] Wilson, A.J.C. (1963). *Mathematical theory of X-ray powder diffractometry*. Philips Technical Library.